water

MDPI

Article

Future Runoff and Sediment Dynamics in a Highly Erodible Loess Plateau Watershed Across Alternative Climate and Land-Use Pathways

Hongfei Yang [1,2,†], Ziwei Zhao [1,2,†], Ke Li [3], Kuandi Zhang [1,2,*], Yanqi Zhang [1,2], Jiani Zhao [1,2] and Mingwang Zhang [1,2]

[1] College of Water Resources and Architectural Engineering, Northwest A&F University, Yangling 712100, China; hongfeiy1988@126.com (H.Y.)
[2] Key Laboratory of Agricultural Soil and Water Engineering in Arid and Semiarid Areas, Ministry of Education, Northwest A&F University, Yangling 712100, China
[3] School of Law, Xinjiang University of Political Science and Law, Tumushuke 843900, China
* Correspondence: zhangkuandi428@126.com
† These authors contributed equally to this work.

Abstract

Runoff and sediment regimes in highly erodible watersheds are increasingly affected by concurrent changes in climate and land use. However, runoff and sediment do not necessarily respond synchronously, making future sediment evolution and erosion-control planning difficult to assess. This study integrated Coupled Model Intercomparison Project Phase 6 (CMIP6) projections, the Patch-generating Land Use Simulation (PLUS) model, and the Soil and Water Assessment Tool (SWAT) to investigate historical and future runoff–sediment dynamics in the Wuding River Basin on the Loess Plateau. Meteorological, land-use, runoff, and sediment records for 1961–2021 were used for historical diagnosis and model development. Future simulations for 2022–2045 considered three Shared Socioeconomic Pathway (SSP) climate pathways and four land-use scenarios, including natural development, farmland protection, ecological protection, and urban development. Historical analysis identified asynchronous regime shifts, with runoff changing markedly in 1996 and sediment transport in 2002, respectively. Future runoff and sediment responses also varied among climate pathways. Mean annual runoff changes by +0.15, +0.34, and -0.65×10^8 m^3 under SSP1-2.6, SSP2-4.5, and SSP5-8.5, respectively, while the corresponding sediment changes are -0.01, +0.04, and -0.06×10^8 t, showing that increased runoff does not necessarily lead to increased sediment export. Ecological protection and urban development produce the largest streamflow increases, whereas all land-use scenarios reduce sediment export relative to the 2020 baseline. Strong seasonal concentration persists, with July–October contributing more than 40% of annual runoff and June–September accounting for over 70% of annual sediment transport. These findings provide a quantitative basis for adaptive water resources management and ecological restoration in erosion-prone watersheds.

Keywords: future climate; land-use trajectories; PLUS; SWAT; runoff-sediment dynamics; Wuding River Basin

Check for updates

Academic Editor: Achim A. Beylich

Received: 11 September 2026
Revised: 3 October 2026
Accepted: 7 October 2026
Published: 16 October 2026

Copyright: © 2026 by the authors. Licensee MDPI, Basel, Switzerland. This article is an open access article distributed under the terms and conditions of the Creative Commons Attribution (CC BY) license.

1. Introduction

Global climatic shifts, together with intensifying anthropogenic pressures, are reconfiguring watershed hydrological functioning, erosion processes, and fluvial sediment

dynamics, with far-reaching implications for water security, ecosystem conservation, and sustainable regional development [1,2]. Rising temperatures and intensified extreme rainfall events can affect runoff generation, sediment yield intensity, and the intra-annual distribution of runoff and sediment by altering evapotranspiration, soil moisture, runoff generation mechanisms, and erosion dynamics [3,4]. Meanwhile, human interventions associated with land-system change, ecological restoration, terracing, check-dam construction, and water-resource development can modify basin-scale hydrological and sediment responses by reshaping surface characteristics, flow-routing pathways, and sediment-transfer connectivity [5,6]. Under compound environmental changes, runoff and sediment transport processes no longer exhibit simple linear changes driven by a single climatic factor, but instead exhibit non-stationarity, spatial heterogeneity, and scenario-specific responses arising from the interplay among climatic forcing, land-system evolution, and basin management interventions [7,8].

Scenario-based approaches are widely adopted to investigate future water and sediment behavior at the watershed scale, typically incorporating both climate forcing and land-use evolution. CMIP6 projections from multiple global climate models (GCMs) provide the climatic inputs required for regional assessments, allowing future variations in temperature, precipitation, and other climate variables to be characterized under alternative SSP pathways. For example, Ma et al. [9] compared the responses of runoff and sediment in the upper Mekong River Basin to future climate change based on Coupled Model Intercomparison Project Phase 5 (CMIP5) and CMIP6 models and found that future runoff and sediment loads differ significantly among different climate model ensembles. Legass et al. [10] used CMIP6-driven SWAT+ ensemble simulations and found that risks associated with flooding, dry-season runoff, and sediment export may increase simultaneously under high-emission scenarios. Based on GCM-derived projections, Islam and Chakma [11] examined the long-term evolution of rainfall erosivity in the Jhelum Catchment and found that future shifts in precipitation characteristics could increase erosive rainfall potential across SSP pathways. These studies demonstrate that coupling CMIP6/SSP scenarios with process-based models is an important technical approach for identifying future hydrological and sediment changes and their uncertainties.

At the same time, land-use simulation methods have evolved from quantity prediction to spatial pattern simulation, from independently applied models to interconnected simulation systems, and from static simulation to dynamic patch evolution simulation [12]. The PLUS framework links driver identification with patch-based spatial allocation, enabling the mechanisms of land transformation and the evolution of landscape patterns to be represented simultaneously [13]. Its applications span future land-pattern projection, regional spatial planning, and ecosystem-oriented management [14,15]. Compared with traditional models such as Cellular Automata-Markov (CA-Markov) and the Future Land Use Simulation Model (FLUS), the PLUS model has certain advantages in identifying land-use change mechanisms and characterizing dynamic landscape patch evolution [16]. Ma et al. [17] constructed a GCM-PLUS-SWAT integrated framework to quantify runoff responses arising from the interplay between climate forcing and land-use evolution and found that climate change was the dominant factor affecting runoff change, while land-use change still played a regulating role. He et al. [18] subsequently linked CMIP6-derived climate forcing with PLUS-based land-use projections and SWAT simulations of hydrological and sediment processes and revealed seasonal differentiation and spatial differences in future hydrological and sediment processes under different emission scenarios.

SWAT has been widely used to assess watershed runoff and sediment responses to climate and land-use change [19–23]. Recent studies have combined climate projections and land-use scenarios with SWAT to examine future watershed responses [24–26], while

others have shown that dynamic land-use inputs and the accuracy and spatial resolution of land-use data can affect simulation results [27,28].

Although previous studies have made considerable progress in future hydrological scenario simulation and runoff–sediment response assessment, several limitations remain. First, many previous studies have tended to emphasize either climate forcing or land-use change, whereas their joint influence on basin-scale water and sediment dynamics remains inadequately quantified, and comprehensive analyses of runoff–sediment response mechanisms under the coupled effects of climate change and land-use change remain insufficient [29,30]. Second, some studies have mainly focused on runoff changes, whereas the future response of sediment transport, especially the characteristics of intra-annual sediment concentration periods and differences in sediment responses under different scenarios, has not been fully investigated. In particular, whether future runoff and sediment transport change synchronously or in the same direction across scenarios remains insufficiently examined. Third, in terms of land-use scenario setting, traditional models have limited capability in characterizing the driving forces of land-use change and spatial patch expansion, making it difficult to accurately reflect the effects of land-use pattern evolution under different development modes on watershed runoff and sediment processes. Fourth, research in erosion-prone regions has largely focused on reconstructing historical water–sediment variability and identifying its drivers, whereas forward-looking assessments integrating CMIP6-based climate forcing with alternative land-development pathways remain scarce [31,32].

As a representative highly erodible catchment in the middle Yellow River region, the Wuding River Basin is central to regional efforts aimed at erosion control, ecological rehabilitation, and sustainable development. Evolving climate conditions, together with large-scale conservation programs, ecological restoration, resource exploitation, and urbanization, have progressively reorganized surface characteristics and runoff–sediment coupling within the basin [33]. Most previous work has concentrated on documenting historical water–sediment regime shifts and identifying their drivers through tools such as double-mass analysis, empirical mode decomposition, and the Space-Time Assessment of Runoff and Sediment (STARS) method. However, systematic understanding is still lacking regarding how runoff and sediment transport in the Wuding River Basin will change under future climate scenarios and land-use development modes, whether different land-use scenarios will have consistent regulatory effects on runoff and sediment processes, and whether the intra-annual distribution of runoff and sediment will further change in the future.

To address these gaps, a unified CMIP6–PLUS–SWAT framework is employed to assess future water and sediment responses in the Wuding River Basin across alternative climatic and land-system pathways. Model development and evaluation draw on land-cover information, meteorological records, and monthly streamflow and sediment observations at Baijiachuan Station spanning 1961–2021, while scenario experiments are used to explore basin conditions during 2022–2045. Specifically, the analysis seeks to: (1) characterize projected changes in precipitation, temperature, streamflow, and sediment export across SSP pathways; (2) determine how contrasting land-development trajectories alter basin-scale water and sediment behavior; and (3) identify interannual variability and seasonal redistribution in future hydrological and sediment regimes. By integrating climate projections, land-system simulation, and process-based watershed modeling, this study provides a quantitative basis for anticipating pathway-dependent changes in water availability and sediment pressure and for supporting adaptive water resources management, erosion mitigation, and ecological restoration in erosion-prone watersheds. Section 2 introduces the regional setting, data foundation, and methodological framework. The

resulting projections and associated uncertainties are examined in Section 3, while Section 4 synthesizes the major findings and discusses their relevance to basin management.

2. Materials and Methods

2.1. Regional Setting

Situated in the central Loess Plateau, the Wuding River Basin (Figure 1) spans 107°49′–110°57′ E and 37°06′–39°27′ N, covering approximately 30,261 km^2. The main river channel is about 491.2 km long, while basin elevations vary between 600 and 1800 m. The catchment experiences a semiarid continental climate, with a mean annual temperature of 7.96 °C and average yearly precipitation of 401.23 mm, nearly 75% of which occurs from June to September. Deeply dissected loess terrain and weakly cohesive soils are widespread in the middle and lower basin, where wet-season hillslope runoff promotes substantial erosion. Vegetation is dominated by herbs, shrubs, and conifers. This combination of steep terrain, concentrated rainfall, highly erodible soils, and heterogeneous vegetation contributes to severe soil loss across the catchment [34].

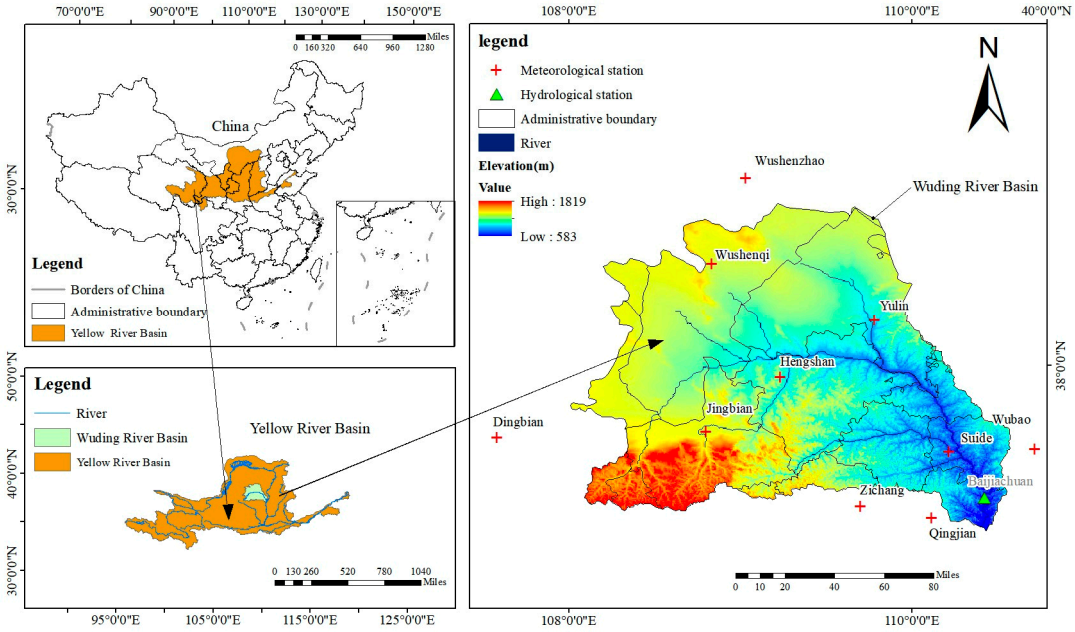


Figure 1. Location and geographic features of the Wuding River Basin.

2.2. Data Sources

Terrain characteristics were derived from a digital elevation model (DEM) with a spatial resolution of 30 m, available through the Geospatial Data Cloud (http://www.gscloud.cn/; accessed on 11 May 2024). Soil data were obtained from the global soil database provided by the Cold and Arid Regions Science Data Center (http://www.ncdc.ac.cn/portal/; accessed on 16 May 2024) at a 1 km spatial resolution. Meteorological data for 1961–2021, including wind speed, temperature, solar radiation, precipitation, and relative humidity, were compiled from records available through the China Meteorological Data Service Centre (http://data.cma.cn/; accessed on 22 May 2024). Land-use and land-cover change (LUCC) data were obtained from the Geographic Monitoring Cloud Platform (http://www.dsac.cn/; accessed on 15 May 2024) at a 30 m resolution. Monthly runoff and sediment data for 1961–2021 at the Baijiachuan Hydrological Station were obtained from hydrological yearbooks for the Wuding River Basin. Future climate model data were obtained from CMIP6 (https://pcmdi.llnl.gov/CMIP6/; accessed on 22 May 2024). Daily precipitation together with mean, maximum, and minimum air temperature constituted the climate

variables used in the analysis. Historical simulations for 1961–2014 served as the reference for bias adjustment of projections for 2015–2045 under SSP1-2.6, SSP2-4.5, and SSP5-8.5. The ensemble incorporated six GCMs: ACCESS-CM2, BCC-CSM2-MR, CNRM-CM6-1, CNRM-ESM2-1, INM-CM4-8, and TaiESM1 [35]. For PLUS land-use prediction, nature reserves and water bodies, as well as raster distances to river systems, administrative settlements, roads, and railways, were compiled using spatial datasets available through the National Catalogue Service for Geographic Information Resources (https://mulu.tianditu.gov.cn/; accessed on 10 May 2024). The socioeconomic inputs comprised 1 km gridded population density and gross domestic product (GDP) datasets supplied by the Resource and Environment Science and Data Center (https://www.resdc.cn/; accessed on 28 May 2024).

2.3. Methodology

Figure 2 outlines the CMIP6–PLUS–SWAT framework for assessing future runoff and sediment responses in the Wuding River Basin. Historical change-point analysis informed the division of SWAT calibration and validation periods. Six GCMs were downscaled using the Delta method, evaluated against observations, and combined through arithmetic averaging to provide climate inputs for 2022–2045 under three SSP pathways. Meanwhile, PLUS integrated development probabilities derived from the Land Expansion Analysis Strategy (LEAS), Markov-based land demands, and transition constraints and neighborhood weights within Cellular Automata based on multi-type Random Seeds (CARS) to generate four land-use scenarios for 2035. These inputs were used to drive the calibrated SWAT model. Climate-related responses were assessed with land use fixed at its 2020 configuration, while land-use effects were evaluated by comparing the 2035 scenarios with the 2020 configuration under identical climate forcing. Annual and monthly outputs were analyzed to identify changes in runoff and sediment magnitude, interannual variability, and seasonal distribution.

2.3.1. Change-Point Tests

Because conclusions from a single change-point method may be accidental, three methods were used to identify change points. The methods were cross-checked to obtain more reliable results.

(1) Moving t-test

For a sequence x containing n observations, each candidate time point is treated as a potential change point, which separates the original sequence into two subseries, x_1 and x_2. Let n_1 and n_2 denote the respective sample sizes of the two subseries, with $\overline{x_1}$ and $\overline{x_2}$ representing their means and s_1^2 and s_2^2 their variances. The moving t-test statistic is then expressed as follows:

$$T = \frac{\overline{x_1} - \overline{x_2}}{s\sqrt{\frac{1}{n_1} + \frac{1}{n_2}}} \quad (1)$$

$$s = \sqrt{\frac{n_1 {s_1}^2 + n_2 {s_2}^2}{n_1 + n_2 - 2}} \quad (2)$$

where the significance level $\alpha = 0.05$, if $|T_i| > t_\alpha$—the critical value—an abrupt change is considered to occur at the division point; otherwise, no abrupt change occurs [36].

(2) Pettitt test

The Pettitt test provides a non-parametric approach for detecting a statistically significant shift in a continuous hydroclimatic time series. By locating the most likely change

point, the analyzed sequence can be partitioned into periods before and after the detected shift. The test procedure starts with the construction of a rank-based sequence:

$$U_{\tau,n} = U_{\tau-1,n} + \sum_{j=1}^{n} \mathrm{sgn}(x_i - x_j)(\tau = 2, 3 \ldots n) \tag{3}$$

If τ satisfies:

$$K_\tau = \max_{1 \le \tau \le n} | U_{\tau,n} | \tag{4}$$

then τ is the change point, and the corresponding significance probability p is:

$$p = 2e^{-6K_\tau^2/(n^3+n^2)} \tag{5}$$

If $p \le 0.05$, it is considered statistically significant.

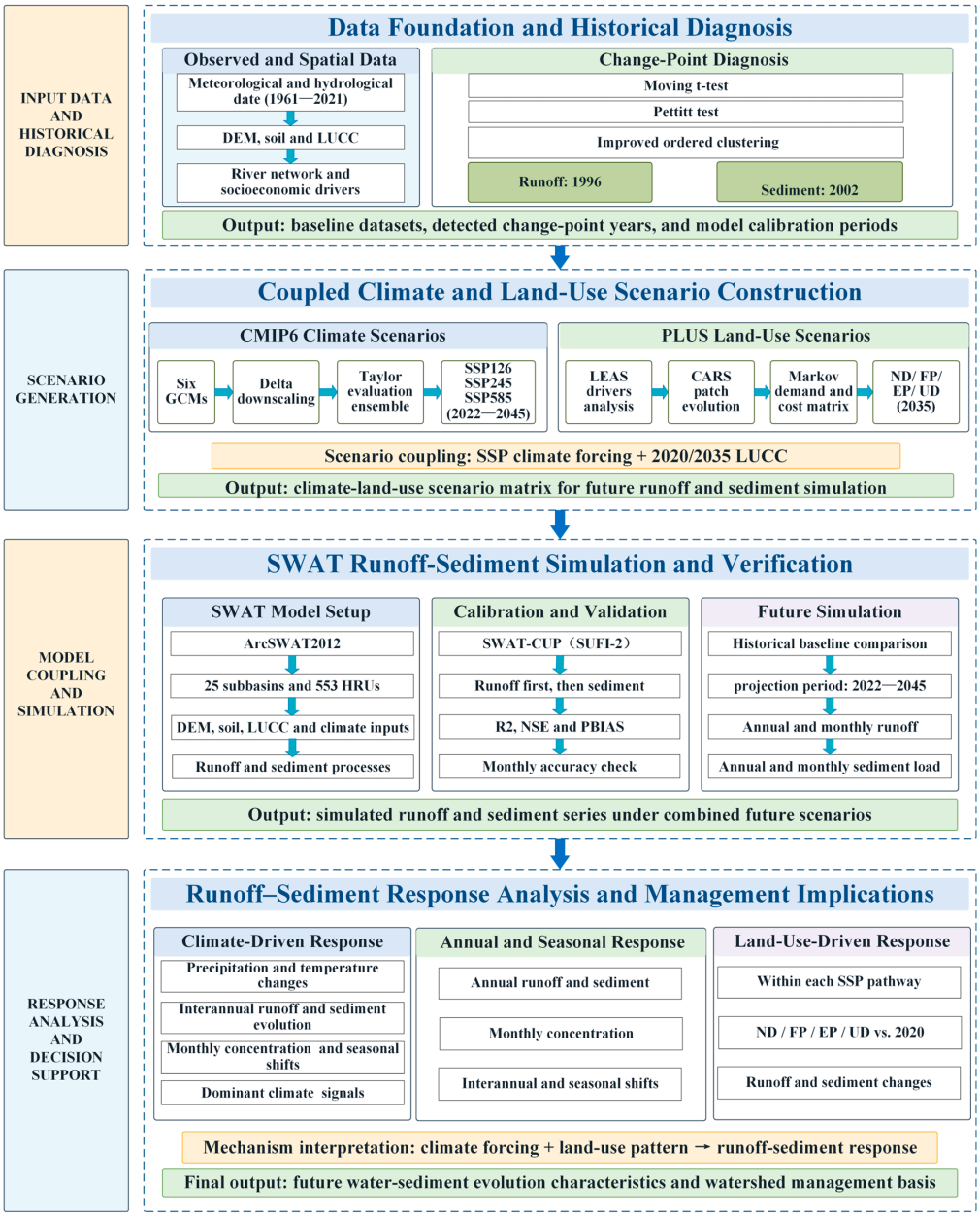


Figure 2. Methodological framework for projecting future runoff and sediment variations in the Wuding River Basin.

(3) Improved ordered clustering method

To overcome the limitation of the traditional ordered clustering method in which the detected change points may be incomplete, an improved ordered clustering method was adopted in this study. Suppose that the most probable abrupt change point in the sequence $\{x_i\}$ ($i = 1, 2,\ldots,n$) is τ. The dispersion between different classes is denoted as d, while the dispersions within the same class are denoted as $\overline{\sigma}_\tau$ and $\overline{\sigma}_{n-\tau}$. The mathematical form of the objective function $S_n(\tau)$ is given by:

$$d = |\overline{x}_\tau - \overline{x}_{n-\tau}| \tag{6}$$

$$\overline{\sigma}_\tau = \sqrt{\sum_{i=1}^{\tau} (x_i - \overline{x}_\tau)^2 / \tau} \tag{7}$$

$$\overline{\sigma}_{n-\tau} = \sqrt{\sum_{i=\tau+1}^{n} (x_i - \overline{x}_{n-\tau})^2 / (n-\tau)} \tag{8}$$

$$S_n(\tau) = \overline{\sigma}_\tau + \overline{\sigma}_{n-\tau} - d \tag{9}$$

When S_n reaches its minimum value, the corresponding $\tau(2 \leq \tau \leq n-1)$ is identified as the abrupt change point.

2.3.2. Downscaling of Global Climate-Model Data

Most GCMs have relatively coarse horizontal spatial resolution, making it difficult to accurately represent local climate evolution. To apply GCM output at the regional scale, this study used the Delta method for downscaling.

$$P = P_{obs,d} \cdot \frac{\overline{P}_{GCM,fut,m}}{\overline{P}_{GCM,ref,m}} \tag{10}$$

$$T = T_{obs,d} + \overline{T}_{GCM,fut,m} - \overline{T}_{GCM,ref,m} \tag{11}$$

In this equation, T indicates air temperature (°C), whereas P denotes precipitation (mm); d and m denote day and month, respectively; $P_{obs,d}$ and $T_{obs,d}$ denote the observed precipitation and air temperature at the meteorological station, respectively; $\overline{P}_{GCM,\,fut,\,m}$, $\overline{P}_{GCM,\,ref,\,m}$, $\overline{T}_{GCM,\,fut,\,m}$, and $\overline{T}_{GCM,\,ref,\,m}$ denote the monthly mean values of the future and historical data from the climate model, respectively.

To further improve the reliability of future climate projections, an arithmetic-mean ensemble was used to integrate the outputs of different climate models, and a standardized Taylor diagram was used to evaluate their simulation performance.

2.3.3. Plus Model

Designed for raster-based land-use modeling, PLUS simulates the emergence and evolution of land patches through two complementary components: LEAS, which explores the drivers of land expansion, and CARS, which reproduces spatial transitions using randomly generated seeds for multiple land-use categories. This integrated structure enhances the model's ability to capture complex land-use change patterns.

The 2035 land-use configuration of the Wuding River Basin was generated through a quantity–spatial allocation procedure within the PLUS framework. Starting from the 2020 land-use pattern, 13 variables representing climatic conditions, terrain characteristics, and socioeconomic influences were incorporated as potential drivers (Table 1). The LEAS component was employed to explore how these variables affected the expansion behavior of individual land categories and to derive class-specific development probabilities. Meanwhile, changes observed between the 2005 and 2020 land-use maps were used to

parameterize a Markov model, from which the required area of each category in 2035 was estimated. Finally, the projected demands were spatially allocated by CARS under the restrictions imposed by the conversion rules (Table 2) and neighborhood interaction coefficients (Table 3), yielding the simulated land-use map for 2035.

Table 1. Explanatory variables incorporated into the PLUS modeling framework.

System Attribute	Data Name	Description
Physical geographic factor	DEM	Elevation of each grid cell
	Slope	Slope of each grid cell
	Aspect	Aspect of each grid cell
Meteorological factor	Precipitation	Long-term average precipitation
	Temperature	Long-term average air temperature
Accessibility factor	Water bodies	Proximity of grid cells to the nearest river network
	Administrative settlements	Proximity of grid cells to the nearest administrative settlement
	Roads	Proximity of grid cells to the nearest road
	Railways	Proximity of grid cells to the nearest railway line
Socioeconomic factor	GDP	Spatial distribution of gross domestic product
	Population density	Spatial distribution of population concentration
Conversion restriction factor	Nature reserves	Shaanxi Yulin Desert National Forest Park, etc.
	Water bodies	Jinjisha, Batuwan, Wanggedu, and other reservoirs

Table 2. Various scenarios of land use conversion cost matrix.

Scenario	**ND**						**FP**					
Land Type	**l_1**	**l_2**	**l_3**	**l_4**	**l_5**	**l_6**	**l_1**	**l_2**	**l_3**	**l_4**	**l_5**	**l_6**
l_1	1	1	1	1	1	1	1	0	0	0	0	0
l_2	1	1	1	0	1	1	1	1	1	0	1	1
l_3	1	1	1	1	1	1	1	1	1	1	1	1
l_4	0	0	1	1	0	0	1	0	1	1	0	0
l_5	1	1	1	0	1	1	0	0	1	0	1	0
l_6	1	1	1	1	1	1	1	1	1	1	1	1
Scenario	EP						UD					
Land type	l_1	l_2	l_3	l_4	l_5	l_6	l_1	l_2	l_3	l_4	l_5	l_6
l_1	1	1	1	1	1	1	1	1	1	1	1	0
l_2	0	1	0	0	0	0	1	1	1	1	1	0
l_3	0	1	1	0	0	0	1	1	1	1	1	0
l_4	0	0	1	1	0	0	0	0	0	1	0	0
l_5	0	1	1	0	1	0	0	0	0	0	1	0
l_6	1	1	1	1	1	1	1	1	1	1	1	1

Note: Land-use classes are represented by l_1–l_6 corresponding sequentially to cropland, forest, grassland, water bodies, built-up land, and unused land. ND, FP, EP, and UD denote the four development pathways considered in this study. Binary values are adopted in the matrix: 1 permits a given land-use transition, whereas 0 prohibits it.

Alternative trajectories of future land development were designed to investigate potential changes in the spatial land-use configuration of the Wuding River Basin. In the PLUS model, the conversion factor is a binary control parameter that determines

whether an existing land-use category can be converted into a target category during CARS spatial allocation. A value of 1 permits the transition, whereas 0 prohibits it, representing a transition constraint rather than a transition probability. These factors were specified based on previous studies, historical land-use transitions, and regional policy requirements, forming the conversion matrices presented in Table 2. Four scenarios were considered: natural development (ND), farmland protection (FP), ecological protection (EP), and urban development (UD).

Table 3. Category-specific coefficients governing local spatial growth.

Land Type	l_1	l_2	l_3	l_4	l_5	l_6
Neighborhood weight	0.87	0.1	0.44	0	1	0.79

Natural development scenario (ND): The projected land-use dynamics were derived from the historical transition characteristics identified over the 2005–2020 period. No additional policy-oriented restrictions beyond the baseline transition rules were imposed.

Farmland protection scenario (FP): Under this pathway, future land allocation was constrained to limit the decline in cultivated area within the Wuding River Basin. Using ND as the reference case, the probability assigned to cropland loss was substantially weakened: conversion to built-up land was reduced by 70%, and conversion to either grassland or water bodies was reduced by 40%. Meanwhile, the transition from unused land to cropland was enhanced by 50%. Together, these parameter changes simulate a development trajectory characterized by stronger protection of agricultural land resources.

Ecological protection scenario (EP): Future land allocation under this pathway was designed to strengthen ecological conservation and suppress excessive expansion of built-up areas. Compared with the baseline configuration, the tendency for cropland to be restored to forest or grassland was enhanced by 20%, while its transition toward construction land was weakened by 30%. Additional constraints were imposed on ecological land loss: the probabilities of forest and grassland being occupied by artificial surfaces were each cut by 20%, and that of water bodies by 40%. Meanwhile, conversion of bare land to construction land was increased by 10%. Key protected zones, such as the Shaanxi Yulin Desert National Forest Park, were incorporated as conversion-restricted areas.

Urban development scenario (UD): Under this pathway, future land allocation favors the expansion of urban and industrial space to reflect a high-intensity regional development pattern. Relative to ND, outward conversion from built-up land to cropland, aquatic areas, forest, grassland, and unused land was suppressed by 40%. At the same time, the attraction of construction land was strengthened by raising the transition likelihoods from cropland, forest, grassland, water bodies, and unused land by 40%, 10%, 20%, 10%, and 50%, respectively.

Neighborhood weights are assigned to quantify the relative propensity of each land-use class to expand into surrounding areas. Based on the experience from previous studies, it was determined according to the land-use changes in the Wuding River Basin and the area change (*TA*) of each land-use type under different preset scenarios (Table 3). The calculation formula is as follows:

$$X_i = \frac{\Delta TA_i - \Delta TA_{min}}{\Delta TA_{max} - \Delta TA_{min}} \quad (12)$$

where X_i refers to the neighborhood coefficient specified for category i; ΔTA_i denotes the area change of category i over the specified period; and $\Delta TA_{\max}$ and $\Delta TA_{\min}$ are the maximum and minimum area changes among all land-use categories, respectively.

2.3.4. SWAT Model

The Soil and Water Assessment Tool (SWAT) model was implemented using ArcSWAT 2012 (Texas A&M University, College Station, TX, USA), an ArcGIS-based interface, to simulate long-term hydrological responses, soil erosion, and sediment transport within the watershed [37]. Runoff simulation: based on hydrological-cycle principles, SWAT commonly uses the Soil Conservation Service (SCS) curve-number method and soil moisture to simulate land-surface runoff. The water balance equation is expressed as follows:

$$SW_t = SW_o + \sum_{i=1}^{t} (R_i - Q_{surf,\,i} - EVA_i - \omega_i - Q_{gw,\,i}) \quad (13)$$

where SW_t is the final soil water content (mm); SW_o is the initial soil-water content (mm); R_i is the amount of precipitation on day i (mm); $Q_{surf,i}$ is the surface runoff on day i (mm); EVA_i is the evaporation on day i (mm); ω_i is the percolation from the soil profile on day i (mm); and $Q_{gw,\,i}$ is the groundwater amount on day i (mm).

Sediment yield at the Hydrologic Response Unit (HRU) scale is estimated in SWAT using the Modified Universal Soil Loss Equation (MUSLE). Rather than relying on a single empirical factor, the calculation integrates information on surface-cover characteristics, the inherent vulnerability of soil to erosion, and storm-related forcing. Sediment output is subsequently determined using the following formulation:

$$sed = 11.8 \cdot \left(Q_{surf} \cdot q^{peak} \cdot area_{HRU}\right)^{0.56} \cdot K \cdot C \cdot P \cdot LS \cdot CFRG \quad (14)$$

where sed is the sediment yield on a given day (t); Q_{surf} is the surface runoff (mm); q^{peak} is the peak runoff rate (m^3/s); $area_{HRU}$ is the HRU area (ha); K, C, P, and LS are the soil erodibility factor, vegetation cover and management factor, soil and water conservation practice factor, and topographic factor in the USLE equation, respectively; and $CFRG$ is the adjustment factor.

Model parameterization for the Wuding River Basin was carried out through the Sequential Uncertainty Fitting version 2 (SUFI-2) scheme available in SWAT-CUP 2012. Sensitivity screening identified 18 parameters primarily associated with runoff processes and 12 linked to sediment dynamics (Table 4), which were subsequently included in the optimization procedure. A stepwise calibration strategy was adopted: hydrological responses were adjusted first, followed by sediment-related processes. The resulting simulations were evaluated using the coefficient of determination (R^2), Nash–Sutcliffe efficiency (NSE), and percent bias (PBIAS) to determine whether the model could adequately reproduce observed water and sediment behavior in the basin [38].

Table 4. Optimized parameter settings for hydrological and sediment processes in SWAT.

Category	Sensitivity Rank	Parameter	Adjustment Method	Calibrated Value
Runoff	1	R__CN2.mgt	−0.5~0.5	−0.1
	2	V__GW_DELAY.gw	0~500	206.09
	3	R__SOL_K().sol	−0.43~1.19	−0.43
	4	V__RCHRG_DP.gw	0~1	0.16
	5	V__TRNSRCH.bsn	0~1	0.17
	6	R__SOL_Z().sol	−0.3~0.5	−0.26
	7	V__SLSUBBSN.hru	10~150	61.46
	8	V__GWQMN.gw	0~5000	4518.02
	9	V__GW_REVAP.gw	0.02~0.2	0.14

Table 4. *Cont.*

Category	Sensitivity Rank	Parameter	Adjustment Method	Calibrated Value
Runoff	10	V__CANMX.hru	0~100	11.8
	11	V__EPCO.hru	0~1	0.38
	12	V__CH_N1.sub	0.01~30	15.53
	13	V__ALPHA_BF.gw	0~1	0.37
	14	V__REVAPMN.gw	0~500	63.76
	15	R__SOL_BD().sol	−0.5~0.5	−0.06
	16	R__SOL_AWC().sol	−1~1	−0.98
	17	R__HRU_SLP.hru	0~1	0.73
	18	V__ALPHA_BNK.rte	0~1	0.78
Sediment	1	V__CH_COV().rte	−0.001~1	0.6
	2	R__USLE_K().sol	0~2	1.82
	3	V__SPEXP.bsn	1~1.5	1.14
	4	V__PRF().bsn	0~2	1.15
	5	V__USLE_C.plant.dat	0.001~0.5	0.4
	6	V__CH_EQN.rte	0~4	0.14
	7	V__RSDCO.bsn	0.02~0.1	0.03
	8	V__LAT_SED.hru	0~5000	4442.62
	9	V__CH_ERODMO().rte	0~1	0.73
	10	V__CH_EROD().rte	−0.05~0.6	0.2
	11	V__USLE_P.mgt	0~1	0.99
	12	R__SLSOIL.hru	−1~1	1

Note: R__ means relative change, V__ means replacement by a given value.

3. Results and Discussion

3.1. Climate Change and Future Projection

The applicability of the six selected models and the arithmetic-mean ensemble in the Wuding River Basin was evaluated by comparing 1961–2014 precipitation and temperature data with observations from meteorological stations. A Taylor diagram was drawn (Figure 3). Overall, downscaled temperature performed better than precipitation. INM-CM4-8 and TaiESM1 showed relatively good applicability in the basin, whereas the precipitation correlation coefficients of the other models were below 0.6. root mean square error (RMSE) values for precipitation and temperature were below 1.0 and 0.3, respectively, indicating relatively accurate simulations, and standard deviation ratio (STDR) values were close to 1.0, indicating good performance. After arithmetic-mean ensemble integration, both precipitation and temperature simulations improved. With similar RMSE and STDR, the ensemble correlation coefficient exceeded that of single models, indicating that the ensemble is generally applicable to meteorological simulation in the Wuding River Basin. On this basis, projections from the individual climate models were averaged to characterize future climatic conditions, and the corresponding outputs are displayed in Figure 4. From the perspective of uncertainty, precipitation projections derived from GCMs generally exhibit greater uncertainty than temperature projections, which is consistent with previous findings. As indicated by the Taylor diagram, the precipitation and temperature changes predicted by the arithmetic-mean ensemble are closer to station observations than those from other GCMs.

As depicted in Figure 4, marked interannual variability characterized both precipitation and temperature over 1961–2021. Basin-wide annual precipitation ranged from 179.38 to 700.15 mm and averaged 401.23 mm, while displaying a modest long-term increase of 0.45 mm/yr. Mean annual temperature varied between 6.51 and 9.35 °C, with an average of 7.96 °C, and exhibited significant warming at 0.03 °C/yr.

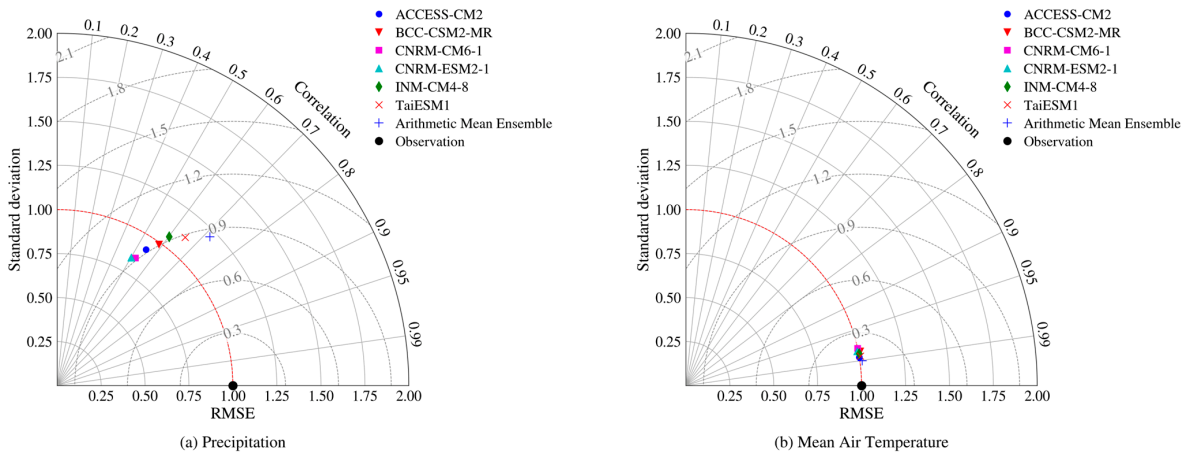


Figure 3. Taylor diagram-based assessment of GCM performance in reproducing precipitation and average temperature.

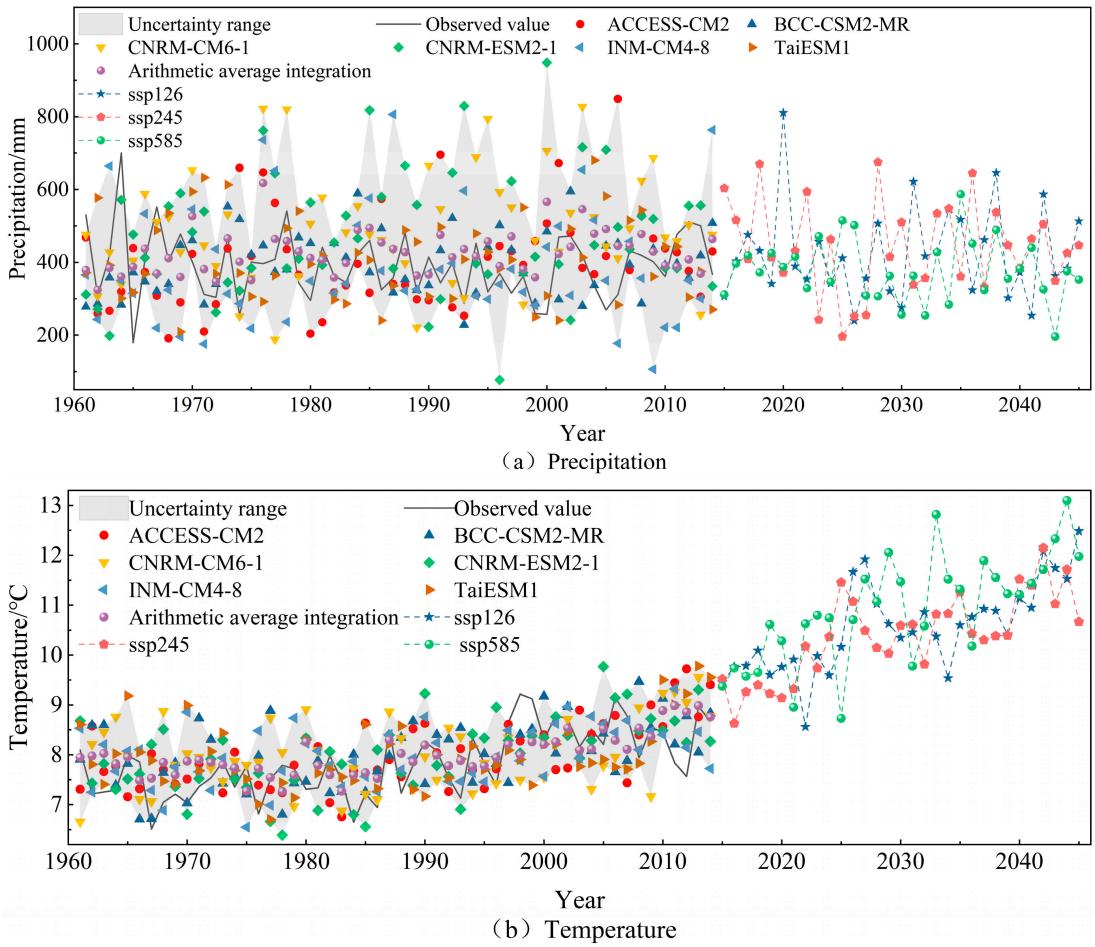


Figure 4. Historical and projected changes in annual precipitation and mean annual temperature in the Wuding River Basin.

Figure 4 illustrates projected changes in precipitation and temperature over 2022–2045 under the three SSP pathways. Compared with the historical period (401.23 mm), the multi-year mean annual precipitation predicted by the arithmetic-mean ensemble is 416.53, 428.09, and 375.21 mm under SSP1-2.6, SSP2-4.5, and SSP5-8.5, respectively. Annual precipitation increases under SSP1-2.6 and SSP2-4.5 by 4% and 7%, respectively, but decreases under SSP5-8.5 by 6%. Compared with the historical mean temperature (7.96 °C), the predicted

multi-year mean temperatures under SSP1-2.6, SSP2-4.5, and SSP5-8.5 are 10.78, 10.73, and 11.23 °C, respectively. Temperature increases under all three scenarios by 2.82, 2.77, and 3.27 °C, respectively, in agreement with earlier findings [39].

3.2. Land-Use Change and Future Projection

Prior to future scenario analysis, a retrospective validation was conducted to examine the predictive reliability of PLUS. The 2005 land-use map served as the initial state for backcasting the spatial pattern observed in 2020, and the output was assessed against the corresponding reference map (Table 5). Model–reference agreement reached 0.87 for the Kappa statistic and 0.91 for overall accuracy. Under the adopted evaluation criterion reported by Li et al. [39], Kappa values of 0.8–1.0 indicate strong spatial agreement. The validation results therefore confirm that PLUS is sufficiently reliable for subsequent projection of land-use dynamics in the Wuding River Basin.

Table 5. Validation metrics for the modeled spatial distribution of land use.

Land Type	Actual Area/(km^2)	Simulated Area/(km^2)	Area Difference/(km^2)	Error/(%)	Kappa	Overall Accuracy
l_1	8156.87	8297.98	141.11	1.73%	0.87	91.43%
l_2	1669.57	1569.57	100	5.99%		
l_3	12,470.07	12,170.07	300	2.41%		
l_4	207.7	247.15	39.45	18.99%		
l_5	443.45	479.54	36.09	8.14%		
l_6	6284.71	6469.77	185.06	2.94%		

The land-cover structure remained strongly concentrated in two major categories throughout 2005–2020 (Figure 5a). Grassland and cropland jointly represented more than 70% of the basin, with mean area fractions of approximately 42% and 28%, respectively. Thus, grassland formed the largest component of the landscape, followed by cropland. This ordering is in agreement with the pattern previously reported by Sun et al. [40].

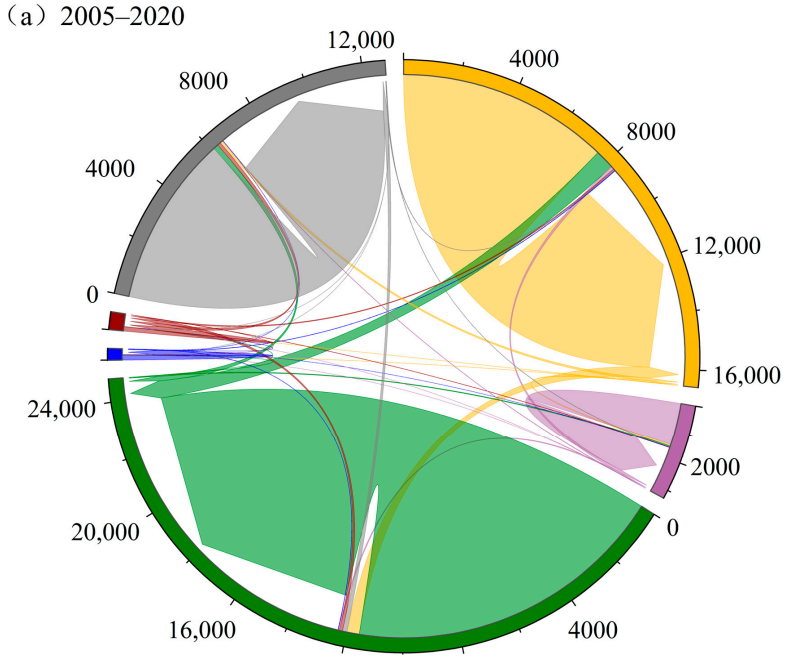


Figure 5. *Cont.*

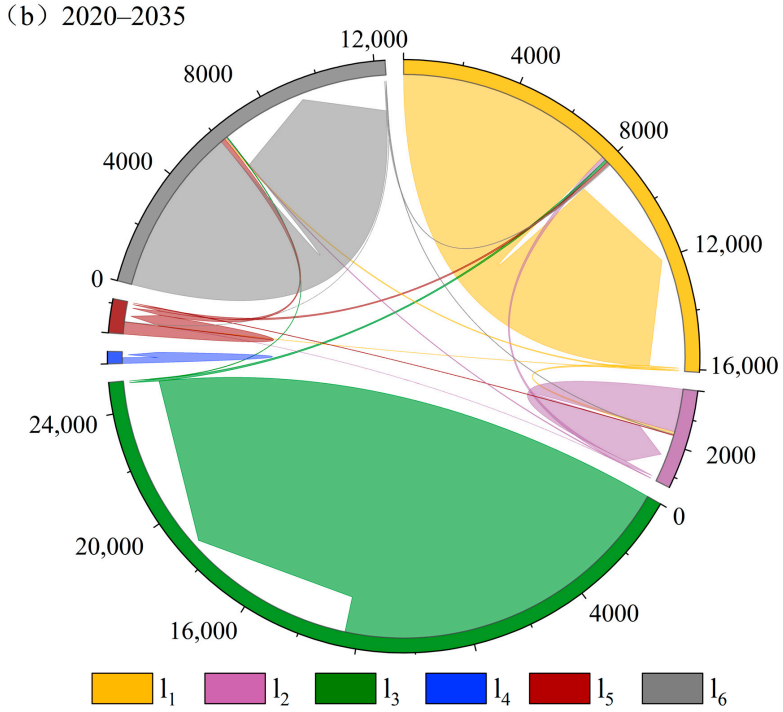


Figure 5. Spatial patterns of land-use transitions in the Wuding River Basin.

As summarized in Table 6, the basin underwent a clear restructuring of its land-use composition between 2005 and 2020. Cropland and unused land contracted, whereas forest, grassland, aquatic areas, and built-up land expanded. The most pronounced increase occurred in built-up land, whose area rose by 176%; approximately 95.5% of this gain was supplied through conversions from cropland, grassland, and unused land. Policy-driven ecological restoration also reshaped cropland transitions, as about 90% of the land leaving cropland was redirected to forest or grassland under the Grain for Green program. Similar conversion characteristics were identified for the subsequent 2020–2035 period (Table 7).

Table 6. Interconversion patterns among land categories during 2005–2020.

Area/(km^2)		2020						Grand Total
		l_1	l_2	l_3	l_4	l_5	l_6	
2005	l_1	7541	107	693	15	47	23	8426
	l_2	60	1500	39	2	11	13	1626
	l_3	443	45	11,546	10	113	158	12,315
	l_4	6	0	6	177	2	2	194
	l_5	5	0	3	0	151	1	161
	l_6	103	16	183	3	119	6088	6512
Grand total		8157	1670	12,470	208	443	6285	29,232

Note: The total area of land-use categories in Table 6 is slightly smaller than the reported watershed area because only valid land-use raster cells within the clipped basin boundary were included in the area statistics. NoData pixels and boundary cells generated during raster clipping were excluded from the calculation.

The projected land-use configuration for 2035 is presented in Figure 6. Expansion of cultivated land is largely observed across the central and downstream sectors, whereas increases in forest cover occur mainly around Zizhou, Qingjian, and Suide counties. Grassland expansion shows no obvious spatial pattern. Construction-land expansion is concentrated mainly in Yuyang District, Hengshan District, and Jingbian County in the middle reaches.

Table 7. Interconversion among land categories under the natural development pathway during 2020–2035.

Area/(km^2)		2035 ND						Grand Total
		l_1	l_2	l_3	l_4	l_5	l_6	
2020	l_1	7776	141	100	0	96	44	8157
	l_2	92	1531	0	0	19	27	1670
	l_3	0	0	12,470	0	0	0	12,470
	l_4	0	0	0	208	0	0	208
	l_5	9	1	0	0	426	8	443
	l_6	52	35	24	0	164	6011	6285
Grand total		7929	1708	12,594	208	705	6090	29,232

Note: Minor discrepancies in row and column totals arise from rounding of cell areas.

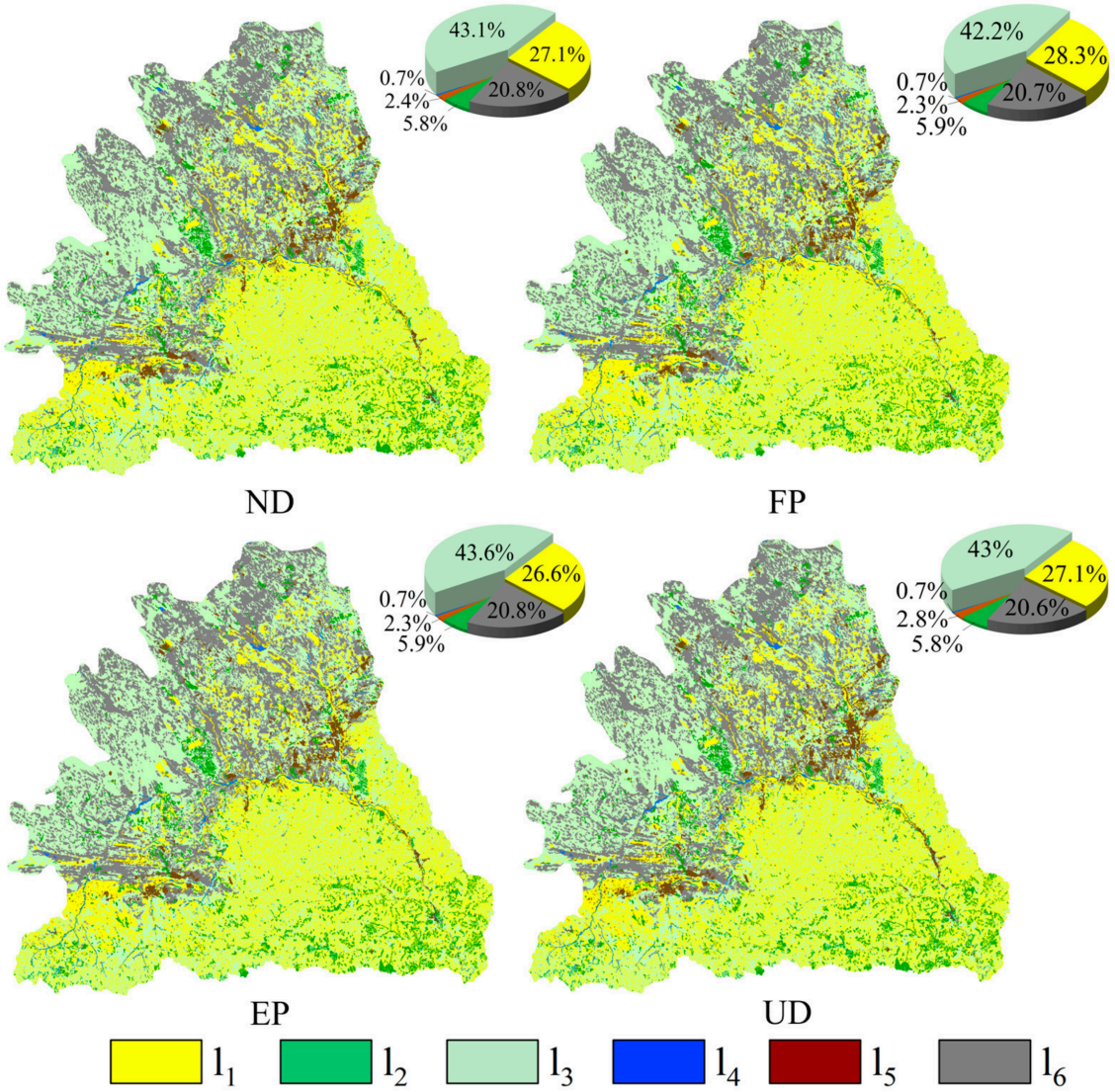


Figure 6. Land use distribution under different scenarios in 2035.

Table 8 summarizes the projected area of each land category across the alternative development pathways for 2035. Cropland increases by 122 km^2 only under the farmland protection scenario and decreases under the other scenarios; the decrease is largest under ecological protection because the influence of Grain for Green regulation is strengthened. Forest land increases under all scenarios. Grassland decreases only under farmland

protection and increases under the other scenarios; forest land and grassland increase most under ecological protection, by 61 km^2 and 279 km^2, respectively. Among the projected pathways, urban development produces the greatest gain in built-up area, which increases by approximately 373 km^2 to 816 km^2, although increases are also observed in the other scenarios.

Table 8. The land use area of each scenario in 2035 in Wuding River Basin.

Category	2020/(km^2)	2035/(km^2)			
		ND	FP	EP	UD
l_1 (Cropland)	8157	7929	8279	7789	7918
l_2 (Forest)	1670	1708	1712	1731	1706
l_3 (Grassland)	12,470	12,594	12,324	12,749	12,565
l_4 (Water bodies)	208	208	208	208	208
l_5 (Built-up land)	443	705	672	677	816
l_6 (Unused land)	6285	6090	6038	6079	6020

3.3. Evaluation of SWAT Simulation Performance

3.3.1. Change Points of Runoff and Sediment Transport

The outcomes of the three change-point detection methods are summarized in Figure 7. Considering the combined evidence, runoff at Baijiachuan Station underwent a major regime shift in 1996, while the corresponding breakpoint for sediment transport was detected in 2002. Notably, the sediment transition lagged the runoff shift by approximately six years, revealing an asynchronous adjustment of water and sediment processes. Such a lag may arise from the buffering effect of sediment storage within slopes and channels, together with delayed changes in sediment supply and transport connectivity. This difference further indicates that alterations in runoff conditions do not necessarily produce an immediate sediment response, highlighting the need to distinguish hydrological variation from sediment-regime adjustment in subsequent model calibration and attribution analysis.

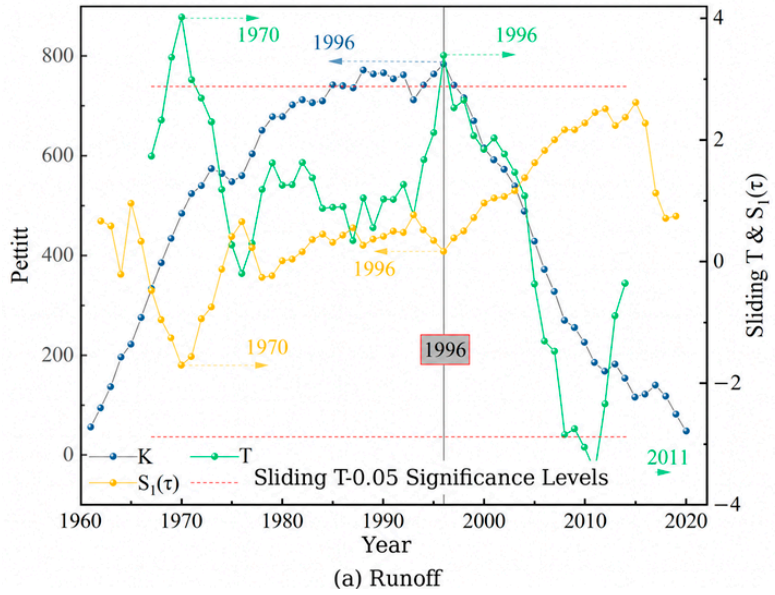


Figure 7. *Cont.*

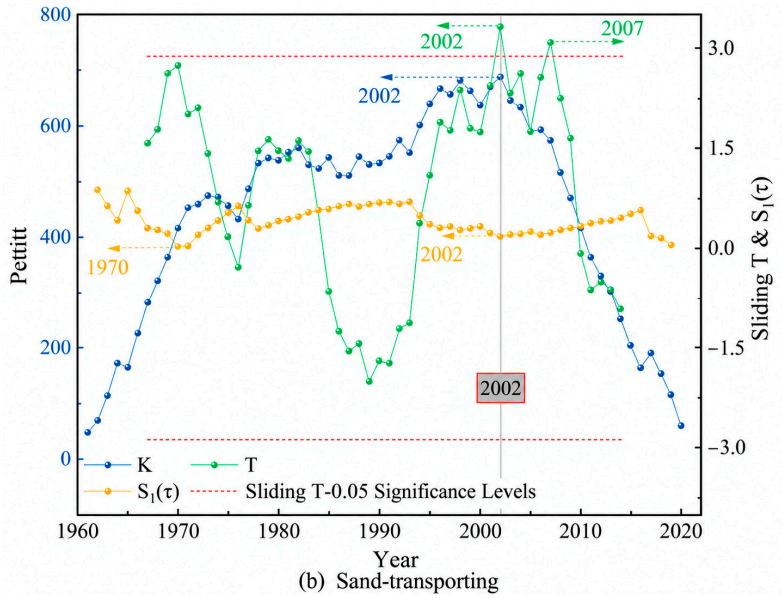


Figure 7. Temporal breakpoints in annual streamflow and sediment transport.

Figure 8 indicates that the timing of large-scale erosion-control activities on the Loess Plateau coincides approximately with the regime transitions detected in the hydrological and sediment series. Within the study basin, terrace construction intensified during the 1990s, while the rapid expansion of check dams mainly occurred before 1990 and slowed thereafter. Continued construction of new structures has been increasingly counterbalanced by the loss of older dams reaching the end of their operational lifespan. As a result, the net functional coverage of check-dam systems has tended to decline, implying a progressive weakening of their overall sediment-trapping effect [41]. At the process level, conservation measures alter surface-flow routing and weaken sediment-transfer continuity between hillslopes and gullies. By changing land-surface properties, limiting erosion, and interrupting the downslope transfer of water and sediment, these measures reduce the amount of material delivered to river channels. Nevertheless, the response is often delayed because the stabilizing effect of hillslope treatments develops gradually rather than instantaneously [42]. This lagged behavior may help explain why the detected breakpoint in sediment transport occurred later than that in runoff at Baijiachuan Station.

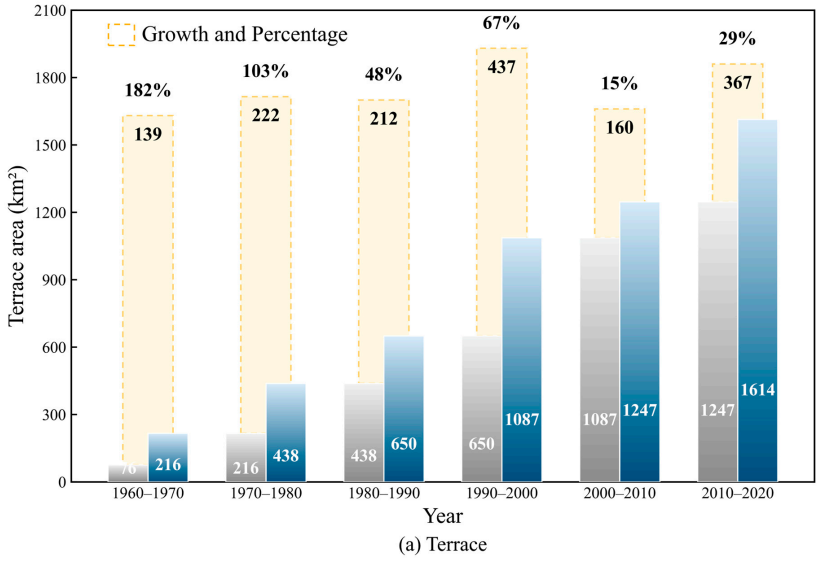


Figure 8. *Cont.*

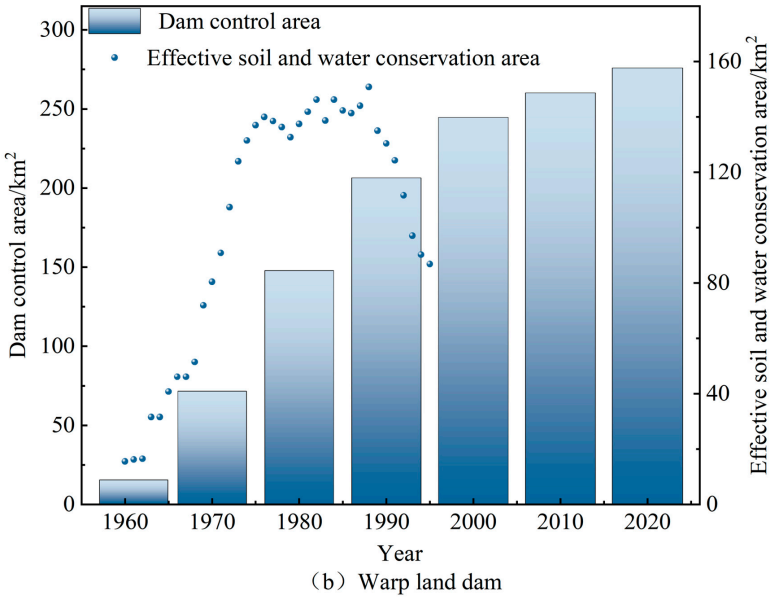


Figure 8. Temporal changes in terrace area and check-dam storage capacity.

3.3.2. Parameter Optimization and Model Performance Assessment

SWAT was implemented at the time step of one month to reconstruct water and sediment processes during 1961–2021. Following identification of the hydrological and sedimentary regime shifts, three years were allocated for model initialization in relation to each breakpoint. The available records were subsequently partitioned at a 7:3 ratio, with the larger subset used for parameter estimation and the smaller subset reserved for independent evaluation. Watershed delineation in ArcSWAT 2012 yielded 25 subwatersheds and 553 HRUs. Simulations were performed using the optimized parameter set reported in Table 4. The simulations reproduced the main temporal behavior evident in the observed records (Figure 9), indicating that the model adequately represented basin-scale hydrological and sediment variability.

Performance statistics for the parameter-estimation and independent-evaluation stages are compiled in Table 9. Streamflow simulations yield R^2 values of 0.713–0.810 and NSE values of 0.697–0.786. Meanwhile, the absolute PBIAS values range from 0.73% to 9.52%, below 15%. For sediment simulation, R^2 and NSE range from 0.685 to 0.873 and from 0.642 to 0.785, respectively, and the absolute PBIAS ranges from 0.296% to 29.854%, below 30%. Because detailed reservoir-operation information was unavailable, reservoir-related parameters were not added to the model. Reservoir operation in SWAT affects runoff and sediment calibration to some extent and therefore influences model performance. Overall, the evaluation metrics suggest that the model provides a reliable representation of monthly hydrological and sediment responses throughout the analyzed periods.

Table 9. Statistical performance of SWAT for monthly streamflow and sediment reproduction.

Period	Simulated Variable	Evaluation Subset	R^2	*NSE*	*PBIAS*
Baseline period	Runoff	Calibration (1964–1986)	0.788	0.786	0.73%
		Validation (1987–1996)	0.743	0.716	−9.52%
	Sediment	Calibration (1964–1990)	0.814	0.754	−19.95%
		Validation (1991–2002)	0.814	0.695	29.85%

Table 9. *Cont.*

Period	Simulated Variable	Evaluation Subset	R^2	*NSE*	*PBIAS*
Post-change period	Runoff	Calibration (2000–2014)	0.810	0.786	−3.39%
		Validation (2015–2021)	0.713	0.697	5.77%
	Sediment	Calibration (2006–2016)	0.685	0.642	−4.69%
		Validation (2017–2021)	0.873	0.785	0.30%

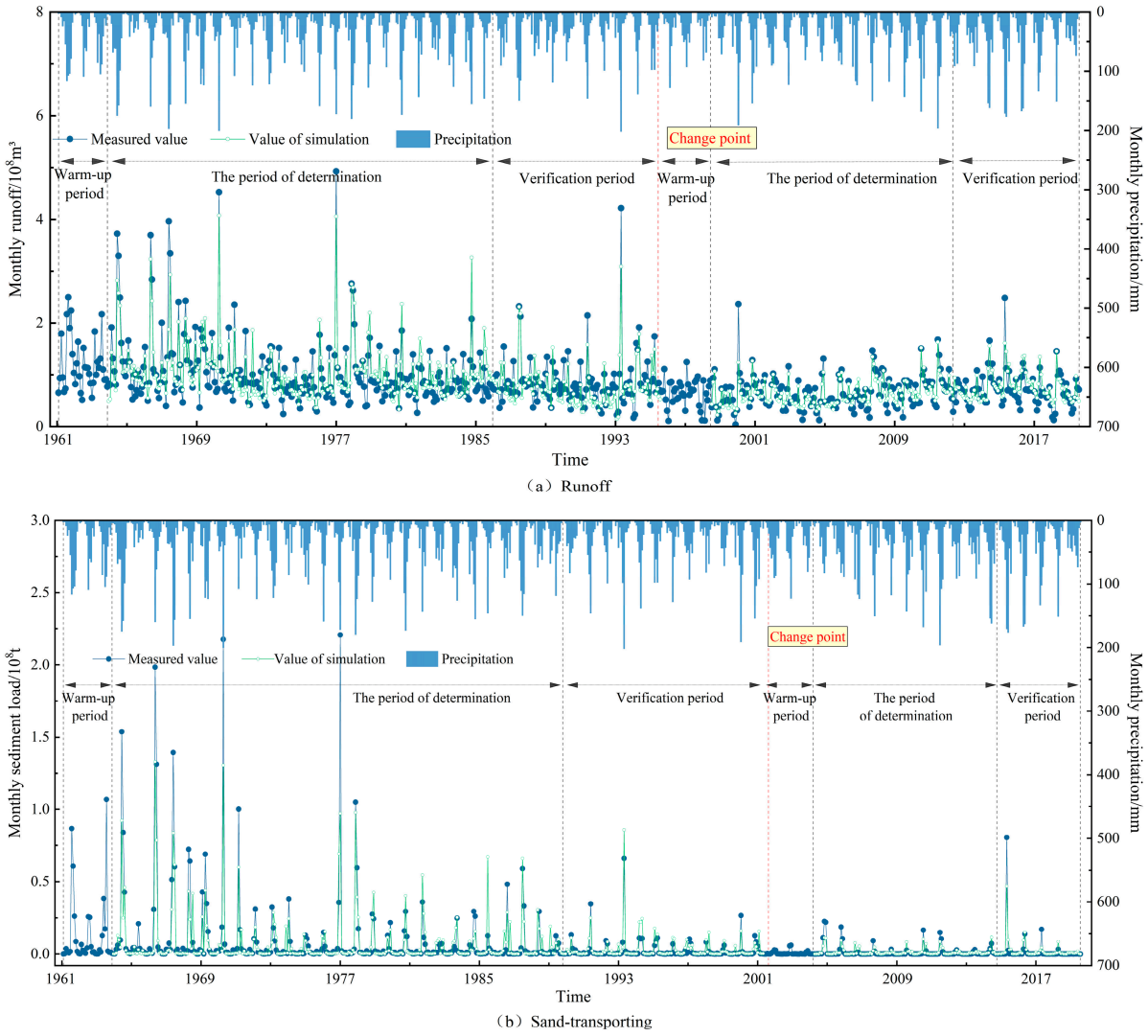


Figure 9. Performance assessment of monthly streamflow and sediment simulations using SWAT.

3.4. Future Runoff and Sediment Response Under a Changing Environment

3.4.1. Runoff-Sediment Relationship Under Climate Change

Controlled scenario experiments were conducted to quantify how projected climatic forcing may alter annual hydrological and sediment dynamics. Land use was fixed at the 2020 pattern, whereas climatic inputs were varied among SSP1-2.6, SSP2-4.5, and SSP5-8.5. Differences in the resulting water and sediment responses are summarized in Figure 10. Runoff increases under SSP1-2.6 and SSP2-4.5 but decreases under SSP5-8.5. Compared with the historical period of 1997–2021 (8.15×10^8 m^3), mean annual runoff increases by 0.15×10^8 m^3 under SSP1-2.6 and 0.34×10^8 m^3 under SSP2-4.5, and decreases by 0.65×10^8 m^3 under SSP5-8.5. Sediment load decreases under SSP1-2.6 and SSP5-8.5 but

increases under SSP2-4.5. Compared with the historical period of 2003–2021 (0.18×10^8 t), multi-year average sediment load decreases by 0.01×10^8 t under SSP1-2.6 and 0.06×10^8 t under SSP5-8.5 and increases by 0.04×10^8 t under SSP2-4.5. Rainfall intensity is the main factor affecting hillslope sediment production. Although precipitation under SSP1-2.6 increases relative to the historical period, causing basin runoff to rise, sediment yield does not increase accordingly, possibly because of the effect of rainfall intensity [43].

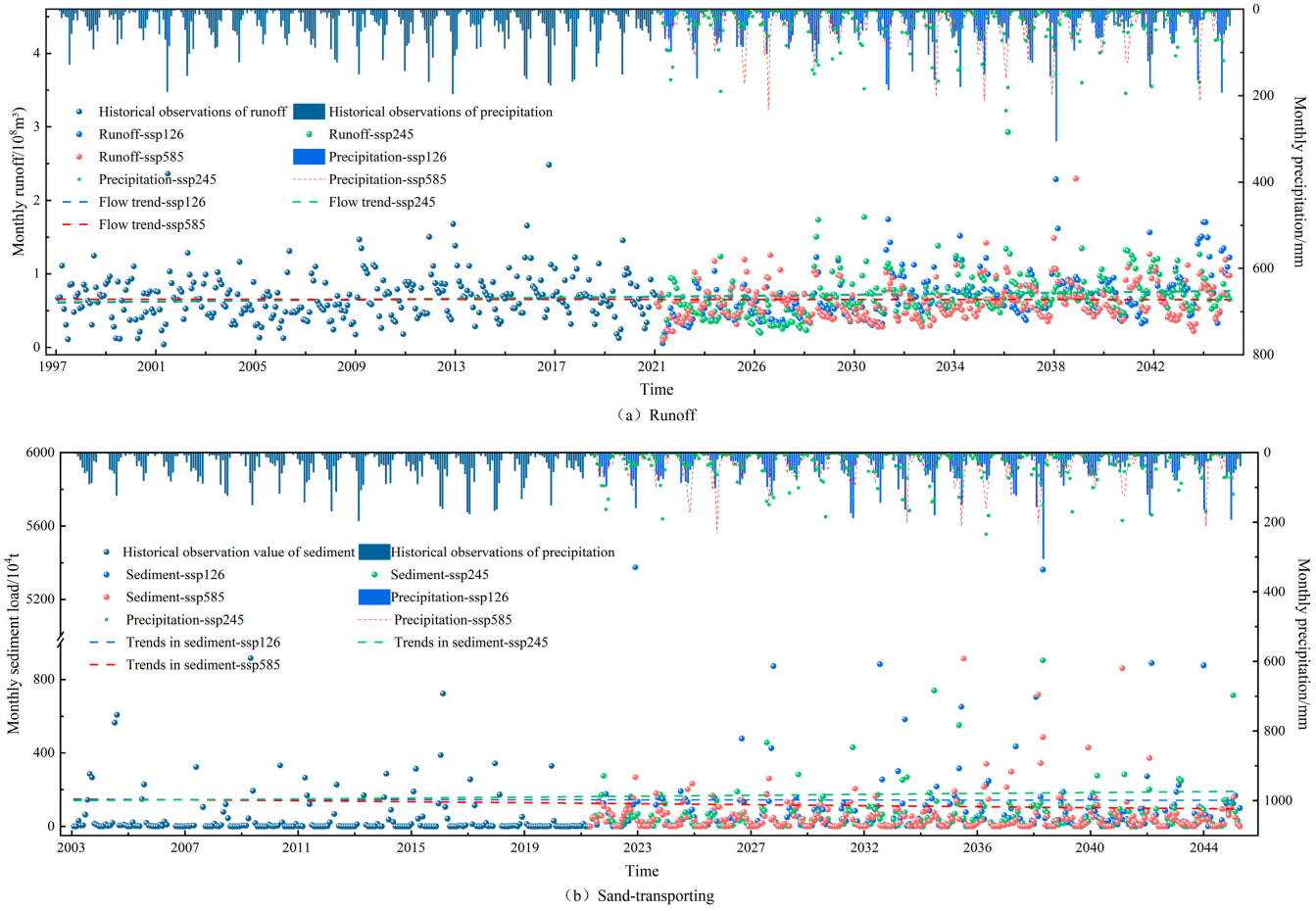


Figure 10. Projected changes in streamflow and sediment transport across SSP pathways.

With SSP5-8.5 adopted as the benchmark pathway, comparative indices were calculated to quantify how streamflow and sediment export respond to changes in precipitation. Positive index values indicate that these variables generally evolve in the same direction. For SSP1-2.6 and SSP2-4.5, the precipitation–runoff indices are 51.58 and 53.36, respectively, whereas the corresponding precipitation–sediment indices are 867.54 and 571.81. The substantial contrast in response magnitude suggests that precipitation is not the sole climatic control on runoff and sediment dynamics, and other meteorological factors may also play important roles [44].

Pronounced seasonal redistribution of water and sediment is evident in Figure 11. Monthly values following the regime shifts, as well as those projected for future periods, are generally below the corresponding pre-shift levels. The hydrological year is dominated by July–October, which collectively contributes more than 40% of annual streamflow, whereas January, April, May, June, and December together account for only around 30%. March forms a distinct secondary peak, supplying roughly one-tenth of the yearly flow, possibly because of snowmelt inputs from upstream areas. Sediment delivery shows a narrower seasonal concentration, with over 70% of the annual total occurring during June–September.

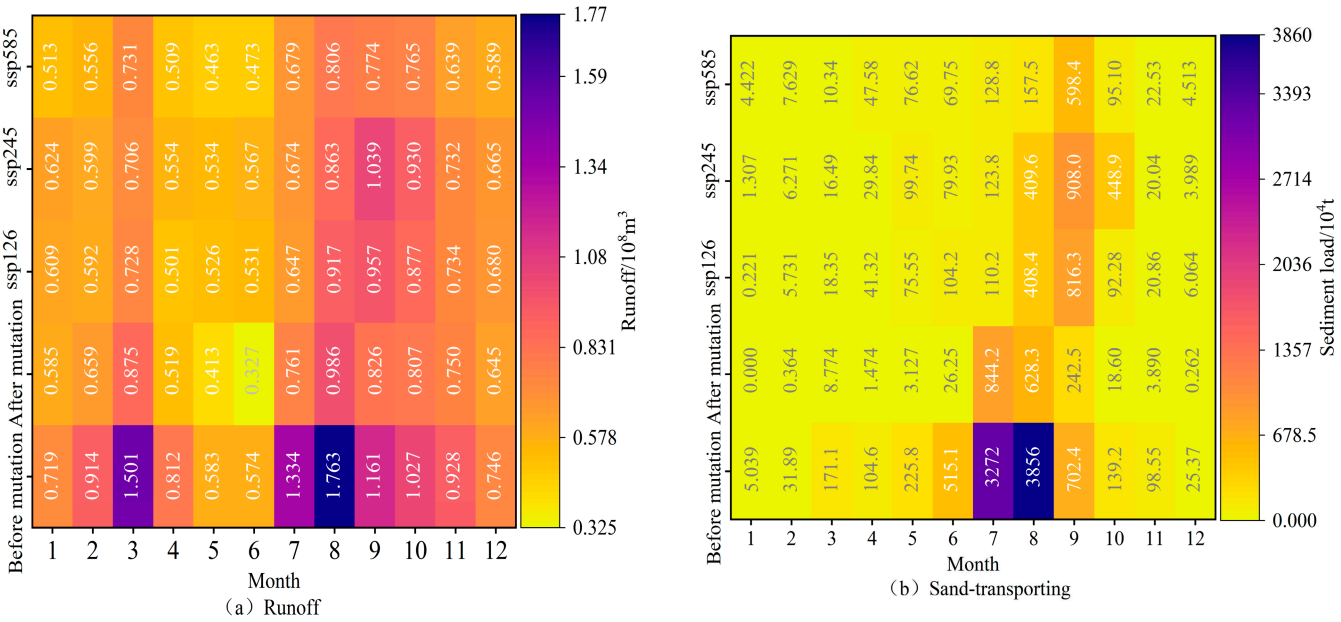
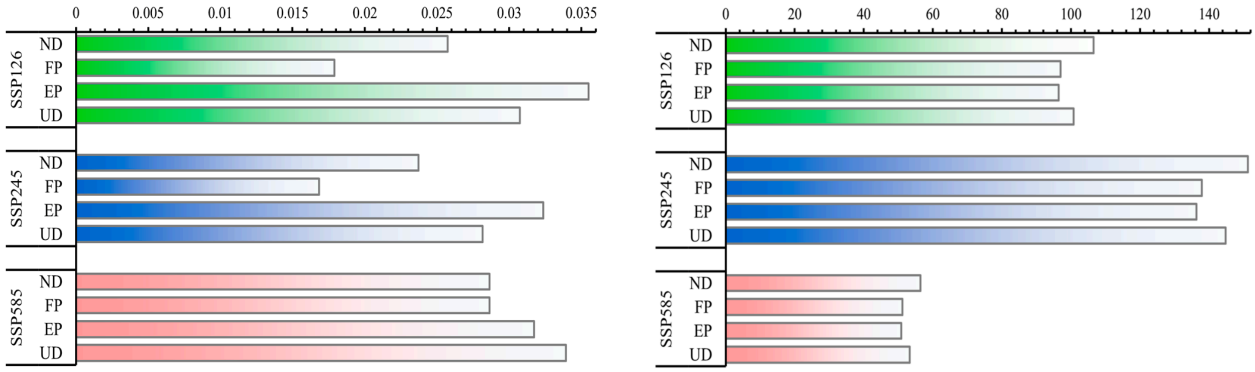


Figure 11. Seasonal patterns of streamflow and sediment transport.

Future seasonal shifts in water and sediment dynamics were evaluated across the three climate pathways, with conditions following the detected regime shifts adopted as the reference state. Under SSP1-2.6 and SSP2-4.5, runoff in February, March, July, and August decreases markedly, by 0.067, 0.147, 0.114, and 0.069 $\times$ 10^8 m^3 and by 0.060, 0.169, 0.087, and 0.123 $\times$ 10^8 m^3, respectively. Runoff in May, June, September, and October increases significantly by 0.113, 0.204, 0.132, and 0.070 $\times$ 10^8 m^3 and by 0.121, 0.240, 0.213, and 0.123 $\times$ 10^8 m^3, respectively. Under SSP5-8.5, only May and June runoff increases significantly, by 0.050 and 0.146 $\times$ 10^8 m^3, while runoff in the other months decreases. The three climate scenarios show generally consistent sediment-load changes, with marked increases in June and September and significant decreases in July and August, consistent with changes reflecting concurrent shifts in the seasonal distribution of streamflow. The sharp decreases in runoff and sediment after the change point are strongly influenced by human activities, with annual means decreasing by 3.91 $\times$ 10^8 m^3 and 0.74 $\times$ 10^8 t, respectively. Monthly values decrease, but the distribution pattern remains unchanged. The scenario comparisons suggest that future water and sediment variability appears to be more strongly governed by climatic forcing than by anticipated land-system shifts.

3.4.2. Impacts of Land-Use Transitions on Streamflow and Sediment Transport

The effects of alternative land-use trajectories on streamflow and sediment transport were evaluated, with the results summarized in Figure 12. Under the same climate scenario, land-use changes in all 2035 scenarios increase runoff relative to 2020 land use, with increases exceeding 0.016 $\times$ 10^8 m^3. The most pronounced streamflow gains occur under the ecological protection and urban development pathways. Under ecological protection, forest land and grassland increase the most, by 61 km^2 and 279 km^2, respectively; cropland decreases the most, by 367.90 km^2; and urban land also increases by 233.43 km^2. Under urban development, cropland decreases by 239.20 km^2, while forest land, grassland, and construction land increase by 36.05, 95.40, and 372.64 km^2, respectively [45]. The natural development and farmland protection scenarios produce smaller runoff increases. Under natural development, no policy restrictions prioritizing specific land types are added, so its effect on runoff is smaller than that of the other scenarios. Under farmland protection, increased cropland and reduced grassland weaken the runoff increase caused by expanded forest cover and built-up areas.



(**a**) Runoff (**b**) Sand-transporting

Figure 12. Streamflow and sediment responses across alternative land-use pathways.

When climate conditions are kept unchanged, all 2035 land-use pathways generate lower sediment export than the 2020 baseline, with declines exceeding 0.5×10^6 t. Under ND, EP, and UD, the contraction of cropland together with the expansion of forest cover, grassland, and built-up areas reduces the potential for sediment production and delivery. FP exhibits a contrasting land-allocation pattern, with more cropland and less grassland; however, increases in forested and developed areas still maintain an overall reduction in sediment output. When evaluated independently, projected land-system changes exert only a modest influence on long-term hydrological and sediment responses, likely owing to the relatively small magnitude of land-area adjustments and limited spatial reorganization across the alternative pathways.

3.5. Uncertainty Analysis

3.5.1. Global Climate Models

Uncertainty in climate projection mainly comes from three sources: scenario uncertainty, uncertainty associated with internal natural variability of the climate system, and uncertainty in representing climate processes. Accurately simulating the climate system and its processes remains challenging. Existing GCMs simplify real climate processes to simulate climate change, and these limitations introduce considerable projection uncertainty. The Delta downscaling method used for climate models also has unavoidable limitations. As an example, downscaling mainly adjusts average and extreme values from the historical series but leaves measures of variability, including the overall spread and variance, essentially unchanged. Another underlying assumption of the Delta approach is that future climate preserves the existing spatial configuration [46]. In addition, using multiple GCM datasets can reduce uncertainty in future runoff and sediment simulation. This study used six GCM datasets. Subsequent studies should incorporate a broader range of climate models and couple different downscaling and ensemble methods to simulate future runoff and sediment more effectively.

3.5.2. Plus Model

Class-specific expansion potential was derived through the LEAS component embedded in PLUS, using 13 predictors that characterize environmental conditions, human activities, and accessibility. Because land-use evolution is governed by multiple interacting mechanisms, projected patterns may inevitably deviate from those that eventually occur. Another source of uncertainty lies in the CARS allocation procedure, where conversion rules and local interaction coefficients must be prescribed in advance. Although these parameters were determined using neighborhood-weight calculation methods reported in previous studies, subjectivity remains to some extent, and further research is needed to

provide more empirical support for parameter selection. As land-use evolution is governed by numerous interacting drivers and constrained by data availability and quantification, it is necessary to optimize driving and restriction factors based on actual development conditions, select more comprehensive driving factors from multiple perspectives, introduce more scientific methods for quantifying drivers, establish more accurate land-use prediction models, and analyze their impacts on future basin runoff and sediment.

3.5.3. SWAT Model

Measured streamflow and sediment records at Baijiachuan Station were used to optimize the SWAT parameter set. Although model performance was satisfactory overall, some discrepancies persisted between the reconstructed series and observations. These deviations may originate from different stages of the modeling workflow, including uncertainties in topographic, land-cover, and soil datasets. Watershed subdivision, inconsistencies in spatial resolution among input layers, and parameter-estimation procedures may also propagate uncertainty into the final simulations [47–50].

Differences in DEM and LUCC resolution are one cause of simulation bias. DEM strongly affects flow convergence and slope, thereby influencing model accuracy. Previous studies found that runoff and sediment load increase as DEM resolution becomes coarser, mainly because DEM resolution affects slope representation. In theory, higher DEM resolution can more realistically represent topography and geomorphology and therefore improve simulation accuracy. Land-use data quality is important for watershed hydrological modeling. Greater spatial detail in land-use inputs can enhance the reliability of runoff simulations by 1.1–6.9%, but overly fine land-use data greatly increase economic and time costs. Some studies also show that land-use accuracy is not strongly correlated with model results. Soil data are essential for SWAT operation and play a major role in shaping hydrological responses and sediment dynamics. SWAT was developed in North America and includes local soil data by default. When applied in China, soil data need additional processing, which introduces uncertainty.

In addition, the effects of reservoirs and check dams on streamflow and sediment retention were not explicitly represented in SWAT, potentially contributing to simulation uncertainty, particularly for sediment.

4. Conclusions

Historical shifts in water and sediment regimes were identified to distinguish the principal evolutionary stages of the observed record. Monthly streamflow and sediment data from Baijiachuan Station for 1961–2021 were then used to develop and evaluate a SWAT-based basin model. Future conditions were investigated through a coupled CMIP6–PLUS–SWAT framework, which integrates SSP climate forcing with alternative land-use trajectories to quantify prospective changes in hydrological and sediment processes. The major outcomes can be summarized as follows:

(1) The annual hydrological and sediment series exhibited major regime transitions in 1996 and 2002, respectively. To account for the different response characteristics of the two processes, SWAT parameter estimation followed a staged procedure in which streamflow-related parameters were optimized before those controlling sediment behavior. Model evaluation at Baijiachuan Station produced R^2 values of 0.713–0.810 and NSE values of 0.697–0.786 for streamflow, whereas sediment results reached 0.685–0.873 for R^2 and 0.642–0.785 for NSE. Overall, the obtained performance statistics demonstrate a reliable representation of monthly hydrological variability and sediment transport.

(2) Model performance was evaluated through a backcasting experiment for 2020. The reconstructed spatial pattern showed strong consistency with the reference dataset, as reflected by a Kappa statistic of 0.87, providing confidence in the use of PLUS for future land-use scenario analysis. Based on this model, land use in the basin was predicted for 2035 under different scenarios. The projected land composition is generally characterized by losses of cropland and unused land and gains in forest, grassland, and built-up areas, whereas water-body extent remains nearly unchanged. The strongest expansion occurs in built-up areas, whereas the overall spatial differentiation among land categories is modest.

(3) Ensemble projections for 2022–2045 suggest that precipitation responses differ among the SSP pathways, whereas warming is common to all three. Relative to the historical baseline, precipitation increases by 15.30 mm in SSP1-2.6 and 26.86 mm in SSP2-4.5 but declines by 26.02 mm in SSP5-8.5. Meanwhile, long-term mean temperature rises by 2.82, 2.77, and 3.27 °C under SSP1-2.6, SSP2-4.5, and SSP5-8.5, respectively.

(4) With land use fixed at its 2020 configuration, projected changes in streamflow and sediment dynamics show that mean annual runoff increases by 0.15×10^8 m^3 and 0.34×10^8 m^3 under SSP1-2.6 and SSP2-4.5, respectively, and decreases by 0.65×10^8 m^3 under SSP5-8.5, relative to 1997–2021. Multi-year average sediment load decreases by 0.01×10^8 t and 0.06×10^8 t under SSP1-2.6 and SSP5-8.5, respectively, and increases by 0.04×10^8 t under SSP2-4.5, relative to 2003–2021. Post-shift and projected conditions are characterized by generally lower monthly water and sediment outputs than the earlier regime. Streamflow is concentrated in July–October, which supplies more than 40% of the annual total, while June–September contributes over 70% of yearly sediment transport. Compared with simulations using 2020 land use under the same climate forcing, EP and UD yield the largest streamflow increases among the 2035 land-use pathways, whereas sediment export declines under all four land-use scenarios (ND, FP, EP, and UD).

Author Contributions: Conceptualization, Z.Z. and K.Z.; methodology, H.Y., Z.Z., K.L., K.Z., Y.Z., and M.Z.; software, H.Y., Z.Z., K.L., Y.Z., J.Z., and M.Z.; formal analysis, J.Z.; validation, K.Z.; resources, K.Z.; writing—original draft preparation, H.Y.; writing—review and editing, K.Z. and M.Z.; funding acquisition, K.Z. All authors have read and agreed to the published version of the manuscript.

Funding: This research was financially supported by the Inner Mongolia Department of Science and Technology 2024 major projects to prevent and control sand demonstration "unveiled marshal" project [grant number 2024JBGS0016]; the National Natural Science Foundation of China [grant numbers 52579077, U2243238]; and the Shaanxi Provincial Water Conservancy Science and Technology Plan Project [grant number 2023skj-5].

Data Availability Statement: The publicly available datasets used in this study can be accessed through the data sources described in Section 2.2. Monthly runoff and sediment data were obtained from published hydrological yearbooks of the Wuding River Basin. Additional information regarding the datasets used in this study can be obtained from the first author upon reasonable request.

Conflicts of Interest: The authors declare no conflicts of interest.

References

1. Fieldhouse, R.; Basu, M. Oceans in Asia smash heat records: What it means for extreme weather. *Nature* **2026**, *654*, 848–849. [CrossRef]
2. Borrelli, P.; Robinson, D.A.; Fleischer, L.R.; Lugato, E.; Ballabio, C.; Alewell, C.; Meusburger, K.; Modugno, S.; Schütt, B.; Ferro, V.; et al. An assessment of the global impact of 21st century land use change on soil erosion. *Nat. Commun.* **2017**, *8*, 2013. [CrossRef]
3. Liu, Q.; Fu, C.B.; Xu, Z.F.; Ding, A.J. Global warming intensifies extreme day-to-day temperature changes in mid-low latitudes. *Nat. Clim. Change* **2026**, *16*, 69–76. [CrossRef]

4. Guan, Y.S.; Gu, X.H.; Slater, L.J.; Li, X.Y.; Li, J.F.; Wang, L.C.; Tang, X.P.; Kong, D.D.; Zhang, X. Human-induced intensification of terrestrial water cycle in dry regions of the globe. *Npj Clim. Atmos. Sci.* **2024**, *7*, 45. [CrossRef]
5. Xu, Z.; Zhang, S.H.; Yang, X.Y. Water and sediment yield response to extreme rainfall events in a complex large river basin: A case study of the Yellow River Basin, China. *J. Hydrol.* **2021**, *597*, 126183. [CrossRef]
6. Heidari, S.; Shourian, M.; Javansalehi, M.; Lotfi, S. Evaluating effect of reservoir operation policy on agricultural water consumption in climate change condition using a socio-hydrological model. *Water Resour. Manag.* **2026**, *40*, 144. [CrossRef]
7. Carter, T.R. The importance of recognizing opportunities in climate change impacts. *Nat. Clim. Change* **2026**, *16*, 525–534. [CrossRef]
8. Mohseni, U.; Agnihotri, P.G.; Pande, C.B.; Durin, B. Understanding the Climate Change and Land Use Impact on Streamflow in the Present and Future under CMIP6 Climate Scenarios for the Parvara Mula Basin, India. *Water* **2023**, *15*, 1753. [CrossRef]
9. Ma, D.; Bai, Z.X.; Xu, Y.P.; Gu, H.T.; Gao, C. Assessing streamflow and sediment responses to future climate change over the Upper Mekong River Basin: A comparison between CMIP5 and CMIP6 models. *J. Hydrol. Reg. Stud.* **2024**, *52*, 101685. [CrossRef]
10. Legass, A.M.; Alamirew, T.; Gebrehiwot, S.G.; Haro-Monteagudo, D. Future hydrological regime shifts and water security risks in Ethiopia's Awash River Basin: Ensemble CMIP6-driven SWAT+ simulations under SSP2-4.5 and SSP5-8.5. *Environ. Chall.* **2026**, *23*, 101523. [CrossRef]
11. Islam, S.U.; Chakma, S. Evaluating the long-term influence of climate change on rainfall erosivity in the Jhelum Catchment: A GCM-based analysis. *Environ. Dev. Sustain.* **2026**, *28*, 7425–7442. [CrossRef]
12. Xia, Y.J.; Dai, W.; Lin, Q.G.; Wang, Y.Q.; Shao, W.; Wang, G.J. The interactive effects of climate and land-use changes on soil water erosion across China under shared socioeconomic pathways. *J. Hydrol.* **2026**, *673*, 135444. [CrossRef]
13. Zhao, N.; Gao, F.; Ma, K.; Teng, Y.; Wan, H.; Wang, J. The Spatio-Temporal Impact of Land Use Changes on Runoff in the Yiluo River Basin Based on the SWAT and PLUS Model. *Water* **2025**, *17*, 1516. [CrossRef]
14. Liang, X.; Guan, Q.F.; Clarke, K.C.; Liu, S.S.; Wang, B.Y.; Yao, Y. Understanding the drivers of sustainable land expansion using a patch-generating land use simulation (PLUS) model: A case study in Wuhan, China. *Comput. Environ. Urban Syst.* **2021**, *85*, 101569. [CrossRef]
15. Liu, J.C.; Liu, B.Y.; Wu, L.J.; Miao, H.Y.; Liu, J.G.; Jiang, K.; Ding, H.; Gao, W.C.; Liu, T.Z. Prediction of land use for the next 30 years using the PLUS model's multi-scenario simulation in Guizhou Province, China. *Sci. Rep.* **2024**, *14*, 13143. [CrossRef]
16. Liu, X.P.; Liang, X.; Li, X.; Xu, X.C.; Ou, J.P.; Chen, Y.M.; Li, S.Y.; Wang, S.J.; Pei, F.S. A future land use simulation model (FLUS) for simulating multiple land use scenarios by coupling human and natural effects. *Landsc. Urban Plan.* **2017**, *168*, 94–116. [CrossRef]
17. Ma, X.N.; Li, Z.B.; Ren, Z.P.; Shen, Z.Z.; Xu, G.C.; Xie, M.Y. Predicting future impacts of climate and land use change on streamflow in the middle reaches of China's Yellow River. *J. Environ. Manag.* **2024**, *370*, 123000. [CrossRef]
18. He, N.; Li, C.; Hao, Y.F.; Guo, W.X.; Zhang, Y.Z.; Tong, F.; Wang, H.X. Unraveling future hydrological and sediment dynamics through an integrated GCMs-PLUS-SWAT coupling framework. *J. Environ. Manag.* **2026**, *404*, 129437. [CrossRef]
19. Wang, H.; Wu, S.Y.; Huang, Y.X.; Liang, T.; Cheng, W.J.; Zhang, L.B. Decomposing multisource uncertainties in ecosystem service assessment: A quantitative framework and application to water conservation in the Three-River-Source Region of China. *Water Res.* **2026**, *300*, 125947. [CrossRef]
20. Zhang, T.P.; Yan, T.Z.; Li, H.; An, M.Y.; Du, X.Z.; Lei, Q.L.; Liu, H.B. Assessing climate change impact on watershed hydrological processes and stream temperature by considering CO2 emissions. *Water Res.* **2025**, *286*, 124161. [CrossRef]
21. Liu, T.; Si, Z.; Liu, Y.; Wang, L.; Zhao, Y.; Wang, J. Runoff and Drought Responses to Land Use Change and CMIP6 Climate Projections. *Water* **2025**, *17*, 1696. [CrossRef]
22. Yang, H.T.; Sun, H.; Jia, C.; Yang, T.; Yang, X. Future climatic projections and hydrological responses with a data driven method: A regional climate model perspective. *Water Resour. Manag.* **2024**, *38*, 1693–1710. [CrossRef]
23. Zhang, Q.Y.; Wu, J.H.; Wang, T.L.; Tang, C.Z.; Liu, W.B. Coupling SWAT and interpretable deep learning to improve streamflow simulation in arid regions. *Water Resour. Manag.* **2026**, *40*, 56. [CrossRef]
24. Wu, X.X.; Zhao, X.H.; Chen, P.; Zhu, B.W.; Cai, W.J.; Wu, W.Y.; Guo, Q.C.; Iribagiza, M.R. Assessing the effects of combined future climate and land use/cover changes on streamflow in the Upper Fen River Basin, China. *J. Hydrol. Reg. Stud.* **2024**, *53*, 101853. [CrossRef]
25. Ji, G.X.; Lai, Z.Z.; Xia, H.B.; Liu, H.; Wang, Z. Future runoff variation and flood disaster prediction of the Yellow River Basin based on CA-Markov and SWAT. *Land* **2021**, *10*, 421. [CrossRef]
26. Yu, X.; Xie, X.H.; Meng, S.S. Modeling the responses of water and sediment discharge to climate change in the Upper Yellow River Basin, China. *J. Hydrol. Eng.* **2017**, *22*, 05017026. [CrossRef]
27. Yang, Q.Y.; Li, X.G.; Sun, J.; Su, X.B. Soil erosion simulation using a novel dynamic LULC SWAT model in the Qinjiang River Basin, Southern Guangxi, China. *J. Hydrol. Reg. Stud.* **2026**, *64*, 103308. [CrossRef]
28. Zhang, L.H.; Deng, C.; Wei, J.; Zou, J.C. Assessing the impacts of climate change and land use/land cover data characteristics on streamflow using the SWAT model in the Upper Han River Basin. *J. Hydrol. Reg. Stud.* **2025**, *61*, 102764. [CrossRef]

29. Choudhary, P.; Devatha, C.P.; Azhoni, A. Simulating streamflow scenarios using hydrological modeling integrated with future land use and CMIP6 climate projections. *Water Resour. Manag.* **2026**, *40*, 103. [CrossRef]
30. Zhang, J.L.; Shang, Y.Z.; Liu, J.Y.; Fu, J.; Wei, S.T.; Tong, L. Causes of variations in sediment yield in the Jinghe River Basin, China. *Sci. Rep.* **2020**, *10*, 18054. [CrossRef]
31. Wang, Z.J.; Xu, M.Z.; Liu, X.; Singh, D.K.; Fu, X.D. Quantifying the impact of climate change and anthropogenic activities on runoff and sediment load reduction in a typical Loess Plateau watershed. *J. Hydrol. Reg. Stud.* **2022**, *39*, 100992. [CrossRef]
32. Zhang, X.; She, D.L. Quantifying the sediment reduction efficiency of key dams in the Coarse Sandy Hilly Catchments region of the Yellow River basin, China. *J. Hydrol.* **2021**, *602*, 126721. [CrossRef]
33. Yao, J.W.; Li, Z.B.; Zhu, B.; Zhang, P.; Wang, J.S.; Sun, W.Y.; Mei, S.S.; Zhang, Y.Q.; Xiao, P.Q. Transformative trends in runoff and sediment dynamics and their influential drivers in the Wuding River Basin of the Yellow River: A comprehensive analysis from 1960 to 2020. *Water* **2024**, *16*, 26. [CrossRef]
34. Shi, C.X.; Zhou, Y.Y.; Fan, X.L.; Shao, W.W. A study on the annual runoff change and its relationship with water and soil conservation practices and climate change in the middle Yellow River basin. *Catena* **2013**, *100*, 31–41. [CrossRef]
35. Li, M.; Di, Z.H.; Duan, Q.Y. Effect of sensitivity analysis on parameter optimization: Case study based on streamflow simulations using the SWAT model in China. *J. Hydrol.* **2021**, *603*, 126896. [CrossRef]
36. Zhang, J.; Ju, X.; Wang, S.; Li, F.; Zhao, Z. Variations in Precipitation at the Shimantan Reservoir, China. *Water* **2023**, *15*, 4313. [CrossRef]
37. Zeiger, S.J.; Hubbart, J.A. A SWAT model validation of nested-scale contemporaneous streamflow, suspended sediment and nutrients from a multiple-land-use watershed of the central USA. *Sci. Total Environ.* **2016**, *572*, 232–243. [CrossRef]
38. Alejo, L.A.; Ella, V.B.; Saludes, R.B. Applicability of the Climate Hazards Group Infrared Precipitation with Stations as rainfall input for SWAT watershed modeling. *Water Resour.* **2021**, *48*, 925–935. [CrossRef]
39. Li, H.; Mu, H.X.; Jian, S.Q.; Li, X.A. Assessment of rainfall and temperature trends in the Yellow River Basin, China from 2023 to 2100. *Water* **2024**, *16*, 1441. [CrossRef]
40. Sun, T.Y.; Ni, M.X.; Yang, Y.N.; Fang, Y.; Xia, J.X. Spatiotemporal changes and driving factors of land use/land cover (LULC) in the Wuding River Basin, China: Impacts of ecological restoration. *Sustainability* **2024**, *16*, 10453. [CrossRef]
41. Han, J.Q.; Gao, J.N.; Luo, H. Changes and implications of the relationship between rainfall, runoff and sediment load in the Wuding River basin on the Chinese Loess Plateau. *Catena* **2019**, *175*, 228–235. [CrossRef]
42. Zhang, S.Y.; Zhao, G.J.; Mu, X.M.; Tian, P.; Gao, P.; Sun, W. Changes in streamflow regimes and their responses to different soil and water conservation measures in the Loess Plateau watersheds, China. *Hydrol. Process.* **2021**, *35*, e14401. [CrossRef]
43. Zhang, Q.W.; Wang, Z.L.; Wu, B.; Shen, N.; Liu, J. Identifying sediment transport capacity of raindrop-impacted overland flow within transport-limited system of interrill erosion processes on steep loess hillslopes of China. *Soil Tillage Res.* **2018**, *184*, 109–117. [CrossRef]
44. Liu, J.Y.; Zhang, Q.; Singh, V.P.; Shi, P.J. Contribution of multiple climatic variables and human activities to streamflow changes across China. *J. Hydrol.* **2017**, *545*, 145–162. [CrossRef]
45. Shi, P.; Zhang, Y.; Ren, Z.P.; Yu, Y.; Li, P.; Gong, J.F. Land-use changes and check dams reducing runoff and sediment yield on the Loess Plateau of China. *Sci. Total Environ.* **2019**, *664*, 984–994. [CrossRef]
46. Diaz-Nieto, J.; Wilby, R.L. A comparison of statistical downscaling and climate change factor methods: Impacts on low flows in the River Thames, United Kingdom. *Clim. Change* **2005**, *69*, 245–268. [CrossRef]
47. Camargos, C.; Julich, S.; Houska, T.; Bach, M.; Breuer, L. Effects of input data content on the uncertainty of simulating water resources. *Water* **2018**, *10*, 621. [CrossRef]
48. Fan, J.H.; Galoie, M.; Motamedi, A.; Huang, J. Assessment of land cover resolution impact on flood modeling uncertainty. *Hydrol. Res.* **2021**, *52*, 78–90. [CrossRef]
49. Jin, X.; Jin, Y.X.; Yuan, D.H.; Mao, X.F. Effects of land-use data resolution on hydrologic modelling: A case study in the upper reach of the Heihe River, Northwest China. *Ecol. Model.* **2019**, *404*, 61–68. [CrossRef]
50. Fisher, J.R.B.; Acosta, E.A.; Dennedy-Frank, P.J.; Kroeger, T.; Boucher, T.M. Impact of satellite imagery spatial resolution on land use classification accuracy and modeled water quality. *Remote Sens. Ecol. Conserv.* **2018**, *4*, 137–149. [CrossRef]

Disclaimer/Publisher's Note: The statements, opinions and data contained in all publications are solely those of the individual author(s) and contributor(s) and not of MDPI and/or the editor(s). MDPI and/or the editor(s) disclaim responsibility for any injury to people or property resulting from any ideas, methods, instructions or products referred to in the content.